PERFORMANCE OF ASYMMETRIC PROPELLERS UNDER VARYING BLADE SPACING

Dima Usov, The University of Manchester, Manchester, U.K.
Timotheos Chronis, The University of Manchester, Manchester, U.K.
Antonio Filippone, The University of Manchester, Manchester, U.K.

Abstract

This paper investigates the performance of two-bladed, radially asymmetric propellers with uneven blade spacing during axial flight. The study's objective is to analyse the impact of blade spacing on thrust, power, and propulsive efficiency in a two-bladed asymmetric propeller. To achieve this, three asymmetric propellers were simulated using the free-vortex wake method, varying blade spacing from 30 to 90 degrees. The study compared the outcomes of the simulations to those of a reference propeller to identify any possible variations in performance. The results indicated only a slight change in overall propeller performance. It was determined that the marginal deterioration in the performance of the propeller was the consequence of the aerodynamic interference effects between the blades, which ultimately offset each other. Therefore, if such propeller geometries offer benefits beyond performance, it is sensible to utilise them.

1. NOTATION

Symbols

c	Blade section chord, m
C_d	Blade section profile drag coefficient
$C_{l,\max}$	Blade section maximum lift coefficient
$C_{l,\alpha}$	Lift-curve slope, 1/rad
C_P	Propeller power coefficient
D	Propeller diameter, m
J	Propeller advance ratio
k	Size of cross-validation subsamples
K_T	Propeller thrust coefficient
n	Propeller speed of rotation, rev/s
$\hat{n}$	Panel outward-normal unit vector
r	Nondimension radial coordinate
P	Propeller power, W
R	Blade tip radius, m
$\hat{s}$	Spanwise unit vector along the bound vortex
T	Propeller thrust, N
$\boldsymbol{V}$	Blade section total velocity at the mid-point of the bound vortex, m/s
V	Free-stream velocity, m/s
x, y, z	Global cartesian coordinates, m
α	Blade local angle of attack, deg
β	Blade geometric twist, deg
θ	Collective pitch setting angle, deg
Γ_B	Blade bound circulation, m^2/s
Γ_B^*	Viscosity corrected blade bound circulation, m^2/s
$\Gamma_{\max}$	Maximum circulation, m^2/s
δ_n	Drag polar coefficient
η	Propeller efficiency
ρ	Ambient air density, kg/m^3

Acronyms:

FVW	Free Vortex Wake
UAV	Unmanned Aerial Vehicle
MA	Mean Error
MAE	Mean Absolute Error
MPE	Mean Percentage Error
MAPE	Mean Absolute Percentage Error

2. INTRODUCTION

One novel propeller design that has not received fair attention – is the asymmetric "Hummingbird" propeller designed by "Zipline" for a 23-kilogram rotary-wing UAV. As appears in Figure 1, the asymmetric propeller has scissors-like blades placed at an acute azimuth separation angle with an offset of the aft blade along the axis of rotation. Presumably, a non-lifting body of a certain mass is placed roughly on the outer halve arc in-between two blades to compensate for angular velocity-induced vibrations. The advantage of such a propeller would be lower high-frequency acoustics signatures because of the altered blade passing frequencies as a result of propeller geometries. Reducing noise annoyance could be advantageous to overcome entry barriers to future urban air mobility [1] and aerial robotics services markets.

Although the acoustics of unevenly spaced blades for axial fans and propellers have been well studied [2]–[4], the lack of published studies documenting the aerodynamic performance and acoustics of the Hummingbird propeller does not inspire confidence in this specific design, as it is unclear what performance cost is associated with improved acoustics aspects. Moreover, to the author's knowledge, no studies address the working principles and performance of such rotary devices.

Figure 1 Asymmetric "Hummingbird" propeller by Zipline. The photo is taken from a video by Mark Rober[2].

The current paper delves into the performance characteristics of generic radially asymmetric propellers during axial flight. The principal objective of the study is to elucidate the impact of blade spacing on thrust, power, and propulsive efficiency in a two-bladed asymmetric propeller. Three distinct asymmetric propellers featuring blade spacing ranging from 30 to 90 degrees were simulated using the free-vortex wake method to accomplish this objective. Subsequently, the results were compared to those of a reference propeller to identify potential performance differences.

3. METHODOLOGY

3.1. Blade geometry

The blade geometry was adapted from NACA 5868-R6 blade. This particular blade geometry was selected based on thorough experimental research conducted by the National Advisory Committee for Aeronautics (NACA) during the late 1930s. NACA made available their findings in multiple reports, documenting the performance of this blade design at a sweep of various operating points and geometric parameters.

The availability of open-access literature renders this blade an ideal reference case for the validation procedure of numerical tools. The geometry distribution of NACA 5868-R6 is quite simplistic, allowing for straightforward replication for subsequent numerical analysis.

The blade model was constructed of thin panels, omitting radial and chord-wise thickness distributions. In contrast, the original blade has a constant R.A.F. 6 airfoil profile along the span and variable thickness. The untwisted planform of the blade model is shown in Figure 2.

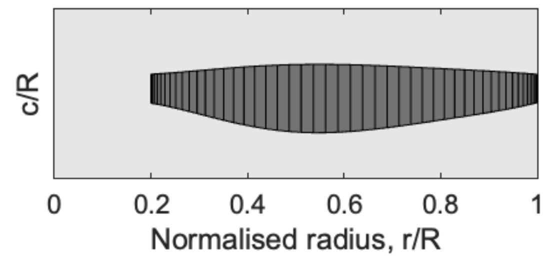

Figure 2 Untwisted planform of the NACA 5868-R6 blade.

There is a lack of clarity as to whether the quarter-chord line of the original blade contains any degree of sweep. Consequently, it has been assumed that the radial sweep of the ¼ chord line is not present.

Figure 3 depicts the distribution of the blade's geometric parameters. The blade radius spans over 1.52 meters, and the root cut-out (hub) is located at 20% of the tip radius along the blade. The geometric twist was configured to enforce zero geometric pitch at the radial section located at 70% of the tip radius at a zero collective setting.

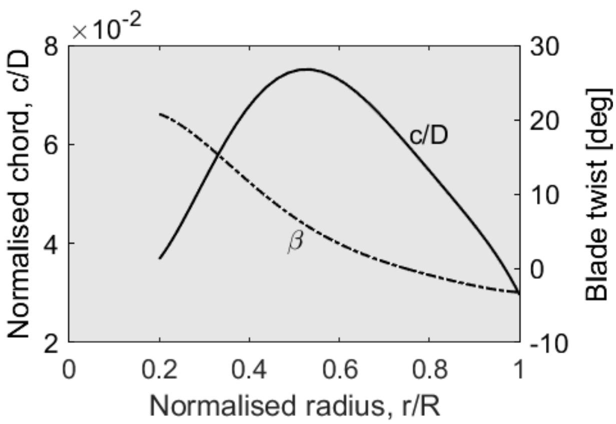

Figure 3 Geometry distribution of the NACA5868-R6 blade. Adapted from Ref. [5].

---

[2] https://www.youtube.com/watch?v=DOWDNBu9DkU&t=831s

3.2. Reference propeller

As mentioned, extensive experimental and theoretical work has been performed on the NACA 5686-R6 bladed propeller. Therefore, despite being a pre-WWII era propeller, it is a rational choice as a reference propeller for comparative studies. The reference propeller geometry "R" is shown in Figure 4.

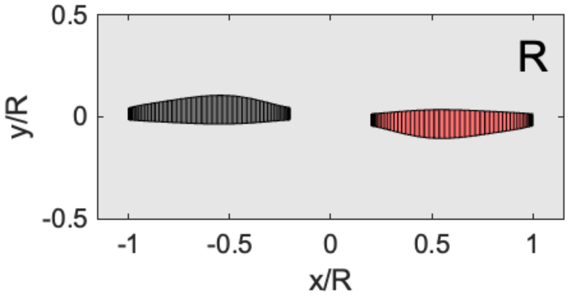

Figure 4 Reference 2-bladed NACA5868-R6 propeller geometry. The trailing blade is illustrated in red colour. Geometry adapted from Ref. [5].

3.3. Asymmetric propellers

A group of three radially asymmetric propellers are considered in the study. All propellers are composed of two NACA 5868-R6 blades having varying azimuth separation angles. The blades shared the same collective setting and angular speed.

In contrast to the Hummingbird propeller, the blades of asymmetric propellers group feature coplanar planes of rotation. This geometric simplification was accomplished to isolate blade spacing effects on propeller performance and allow direct comparison with the reference propeller. Figures 5 - 7 show resultant propeller geometries "A", "B", and "C" with blade azimuth separation of 30, 60, and 90 degrees, respectively.

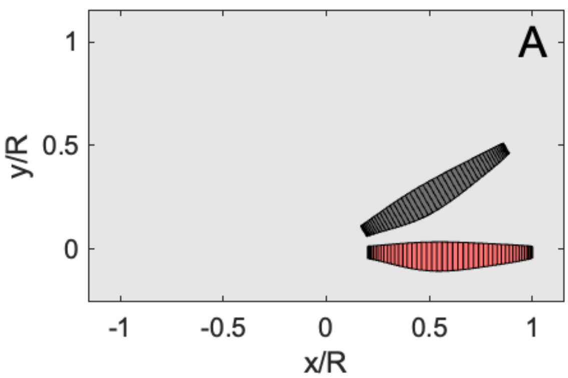

Figure 5 Asymmetric propeller "A" with 30 degrees azimuth separation between the blades. The trailing blade is illustrated in red colour.

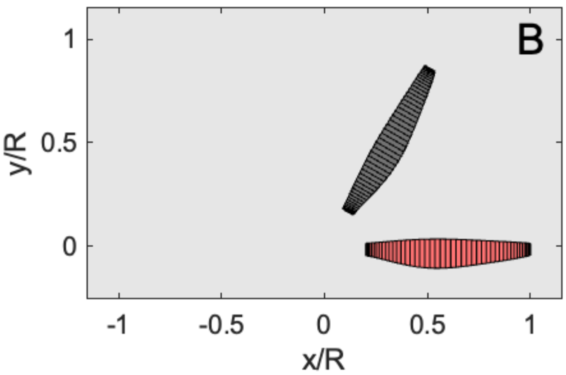

Figure 6 Asymmetric propeller "B" with 60 degrees azimuth separation between the blades. The trailing blade is illustrated in red colour.

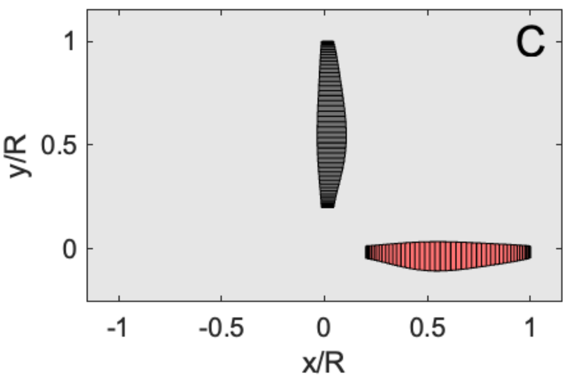

Figure 7 Asymmetric propeller "C" with 90 degrees azimuth separation between the blades. The trailing blade is illustrated in red colour.

3.4. Wake model

The free-vortex wake (FVW) model was used to simulate propeller inflow. The FVW code was developed at the University of Manchester as a part of the U.K. Vertical Lift Network (VLN) MENtOR project Ref. [6]. A detailed description of the FVW model implementation can be found in Ref. [7]. In brief, the model is based on potential flow theory that describes lifting surfaces and their wakes by a lattice of connected vortex filaments, with wake nodes defined at the points where the filaments connect.

Each vortex filament induces a velocity proportional to its strength according to the Biot-Savart law. The sum of the velocities induced from all vortex filaments constitutes the induced velocity at any point. At every time step, the wake nodes are convected by the local instantaneous velocity, which is the sum of the freestream velocity and the total filament-induced velocity.

An initial vortex core radius was set to 10% of the mean bade chord and modelled using the second-order Vatistas vortex core model Ref. [8]. The initial vortex core was allowed to grow based on the Bhagwat-Leishman model, with a turbulent viscosity coefficient, δ, of 1000 Ref. [9].

The positions of the wake nodes were integrated using an *Euler Forward Difference* scheme with a non-dimensional time step corresponding to five degrees change in azimuth angle. The blades were discretised into 50 spanwise and single chordwise panels using cosine distribution to concentrate panels at the root and the tip where higher resolution of blade loads is desired due to high gradients of bound circulation.

3.5. Blade loads model

To obtain the circulation of the bound panels, the flow tangency condition was enforced at the panel centroids. The inviscid and unsteady aerodynamic loads per unit span were calculated according to the equation below from Ref. [10].

$$(1) \qquad \frac{d\boldsymbol{F}}{dt} = \rho\Gamma_B(\boldsymbol{V} \times \hat{s}) + \rho c\left(\frac{\partial\Gamma}{\partial t}\hat{n} + \Gamma\frac{\partial\hat{n}}{\partial t}\right)$$

where ρ is the air density in kilograms per cubic meter; Γ_B is the bound vortex circulation in squared meters per second (m^2/s); Γ is the vortex panel strength in m^2/s; $\boldsymbol{V}$ is the local total velocity at the midpoint of the bound vortex at the quarter chord in meters per second (m/s); $\hat{s}$ is the spanwise unit vector along the bound vortex in meters (m); c is the average panel chord in m; $\hat{n}$ is the outward-normal unit vector of the panels in m, and $\partial/\partial t$ is the first derivative with respect to time, calculated using a first-order backward difference scheme. The Prandtl-Glauert correction factor was applied to the bound circulation to account for compressibility effects.

3.6. Viscous correction

The viscous power losses were accounted for in the postprocessing by estimating profile drag based on the time-accurate, local flow condition along the blade span. A drag polar was estimated by a seventh-order polynomial, e.g.,

$$(2) \qquad C_d = \delta_7\alpha^7 + \delta_6\alpha^6 + \cdots + \delta_0\alpha^0$$

where C_d is the blade section profile drag coefficient; δ_n are drag polar constants obtained by fitting the polynomial to semi-empirical profile drag of R.A.F. 6 airfoil data from Ref. [5]. To clarify, the reported profile drag data was extracted from the propeller thrust measurements. The validity limit of the estimated drag polar was bounded by the reference data domain, between -4 and 16 degrees.

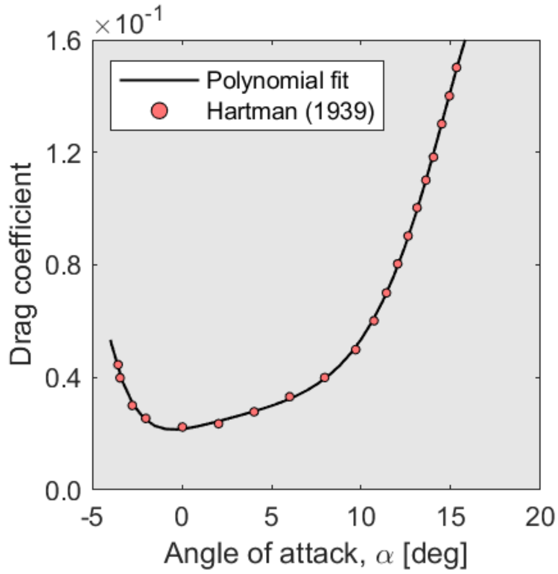

Figure 8 Drag polar of the R.A.F. 6 airfoil and its approximation with a septic polynomial.

The profile drag was updated using the chord-based Reynolds number (Re) correction factor with an exponent of 0.20 based on the expected operational range, Re > 500,000, Ref. [11].

The inviscid blade-bound circulation used in Eq. (1) was corrected by applying a maximum limit based on the maximum lift coefficient and a non-ideal lift-curve slope,

$$(3) \qquad \Gamma_B^* = \frac{C_{l,\alpha}}{2\pi}\Gamma_B \text{ where } C_{l,\alpha} < 2\pi$$

$$(4) \qquad \Gamma_{\max} = \frac{1}{2}\,|\boldsymbol{V}|\,c\,C_{l,\max}$$

$$(5) \qquad \Gamma_B^*(\Gamma_B^* > \Gamma_{\max}) = \Gamma_{\max}$$

where Γ_B^* is the viscosity corrected bound circulation in m^2/s; $C_{l,\alpha}$ is the non-ideal lift curve slope in per radians; $\Gamma_{\max}$ is the maximum bound circulation based on the maximum lift coefficient $C_{l,\max}$ in m^2/s.

Upon introducing the viscous effects, it was noticed that accounting for the corrected bound circulation has a more significant impact on the performance predictions than simply adding viscous power. As shown in Figure 9, correcting inviscid bound circulation reduces the gradient of the thrust coefficient curve and, hence, decreases the induced power. Profile power is accounted for by introducing the viscous drag term, hence increasing the total power.

It was assumed that profile drag does not contribute to the lift based on the small angle theorem.

The format for the aerodynamic coefficients is presented in propeller nomenclature. It is as follows:

$$(6) \qquad K_T = \frac{T}{\rho n^2 D^4}, \qquad C_P = \frac{P}{\rho n^3 D^5}, \qquad J = \frac{V}{nD}$$

where T is the propeller thrust in newtons; n is the propeller rotational rate in revolutions per second; D is the propeller diameter in m; P is the propeller power in watts; J is the advance ratio, and V is the free-stream velocity in m/s.

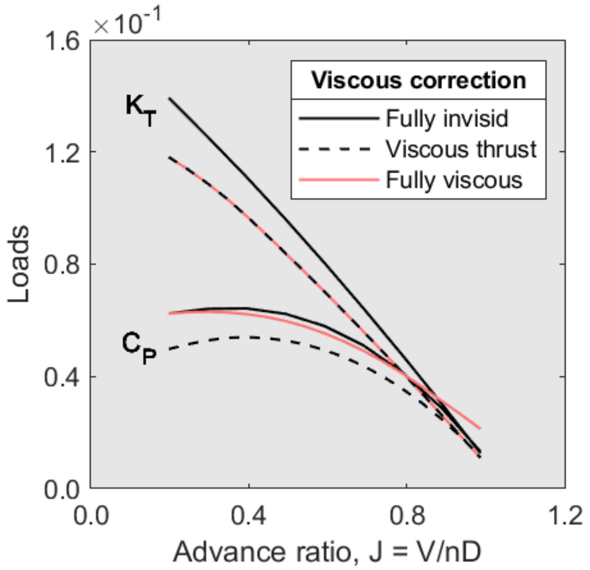

Figure 9 Reference propeller performance predictions at a collective setting of 20 degrees using inviscid and viscosity corrected procedures.

4. VERIFICATION

4.1. Numerical setup

The reference verification case was selected from Ref. [5]. The reference operating case was a 2-bladed NACA 5868-R6 propeller at 20 degrees collective setting for a sweep of advance ratios roughly between 0.1 and 1.1. The propeller angular velocity in the experiment was 1000 rpm which was replicated in a simulation. The simulation length was set to three complete revolutions plus an additional revolution for the spool-up procedure. The near wake was truncated at one revolution into five trailed filaments which represented the far wake.

At the end of each simulation, the local time-accurate blade loads were integrated over the blade span and last revolution to obtain time-averaged values. The advance ratio sweep was covered with 20 operating points, spanning from 7.5 m/s to 55 m/s in 2.5 m/s increments, which roughly corresponds to advance ratios between 0.15 to 1.10.

4.2. Prediction accuracy and data scatter

The predicted performance of the NACA 5868-R6 two-bladed propeller using the free-vortex wake method and wind-tunnel measurements from Ref. [5] are shown in Figure 10. It is important to note that the experimental data have some degree of scatter that cannot be accurately assessed Ref. [5]. The visual assessment indicates good agreement.

To quantify the accuracy of the prediction, it was necessary to interpolate the experimental domain to match advance ratios used in simulations. This was accomplished by fitting polynomials through the data points and evaluating the fitted function at the domain of interest. This procedure introduced an additional error. Ideally, the simulation domain should be set to replicate the domain of the reference experiment. However, provided the fitting error is small, this procedure should hold.

The polynomials were fitted to the experimental data using the *k-fold* (k = 7) cross-validation method to minimise *Mean Absolute Error* (MAE) described in Ref. [12]. Further, the simulation results were compared to the polynomial approximation function based on simulated advance ratios. *Mean Error* (ME) and *Mean Absolute Error* were used as comparison metrics to measure the spread and bias between the simulation and polynomial function. A widely used *Mean Percentage Error* (MPE) and *Mean Absolute Percentage Error* (MAPE) or other relative error functions may not be an appropriate metric for a given data range. Such as when the data values are small or tend to zero at the specific subsets but not across the entire domain Ref. [13]. Nevertheless, the aforementioned metrics are still reported in Appendix Table A1.

Table 1 summarises errors between fitted experimental data polynomial and simulation results. It also presents errors that were introduced during the fitting procedure. The inspection of the results suggests that the simulated thrust and propulsive efficiency were consistently underpredicted throughout the results. In contrast, the errors in power prediction were predominantly due to the spread of the results rather than prediction bias. This offers valuable insight into the action that should be taken to refine the propeller model. However, the model has already demonstrated a satisfactory level of accuracy for the objectives of this work. Further refinement of the model will be conducted outside the scope of the current study.

Table 1 Summary of prediction errors.

Parameter	K_T	C_P	η
ME(P,S)[a]	0.0015	0.0002	0.0302
MAE(P,S)	0.0015	0.0009	0.0302
ME(E,P)[b]	0.0000	0.0000	0.0000
MAE(E,P)	0.0005	0.0004	0.0054

[a] (P,S): fitted polynomial values and simulation results
[b] (E,P): experimental data and fitted polynomial value

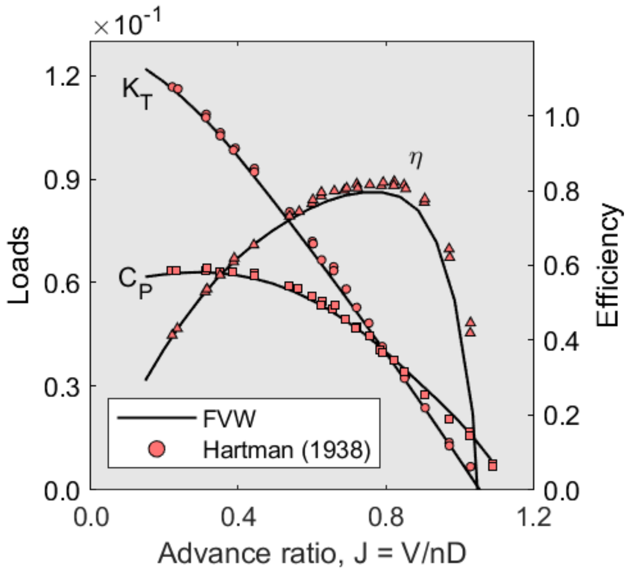

Figure 10 Performance prediction and experimental data from Ref. [5] *of reference propeller at a collective setting of 20 degrees.*

5. RESULTS AND DISCUSSION

5.1. Performance charts

The main results from free-vortex wake simulations are shown in Figures 11 and 12. These figures depict the fundamental performance characteristics of the asymmetric propellers group and the reference propeller: thrust coefficient, K_T; power coefficient C_P, and propulsive efficiency η over a sweep of advance ratios. The propeller performance coefficients were given in Eq. (6), and propulsive efficiency is defined as

$$\eta = \frac{K_T}{C_P} J \qquad (7)$$

Three main observations could be made by examining the results shown in Figures 11 and 12.

1. Blade spacing effects are more apparent at low advance ratios.
2. Reducing the blade spacing degrades the propeller performance.
3. The change in propeller efficiency due to blade spacing is negligible.

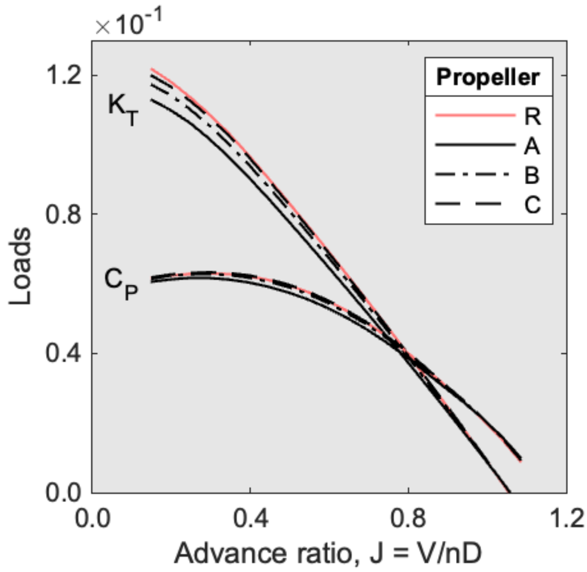

Figure 11 Propeller loads comparison between reference "R" and asymmetric "A", "B", and "C" propellers at a collective setting of 20 degrees.

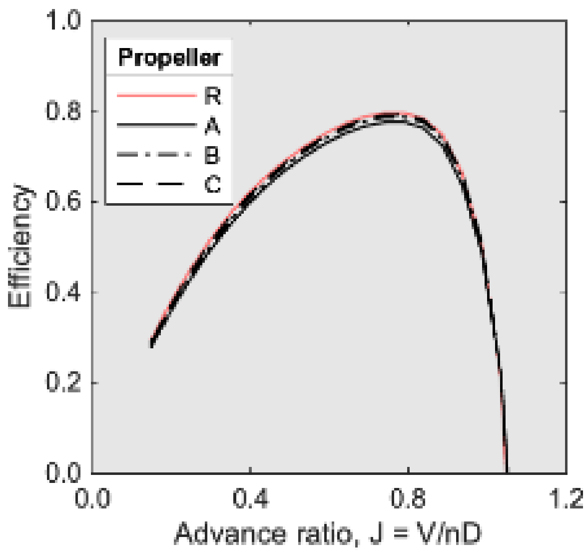

Figure 12 Propeller efficiency comparison between reference "R" and asymmetric "A", "B", and "C" propellers at a collective setting of 20 degrees.

The local perpendicular velocity components at the propeller blades constitute free-stream and induced velocities. At low advance ratios, the dominant component (free-stream) is low, resulting in high local angles of attack and, consequently, higher blade-bound circulation. Ultimately, the increase in the bound circulation is accompanied by increased induction, which is more apparent at small blade spacing.

As the advance ratio increases, the angle of attack decreases. The wakes are convected away faster, and the blades operate as if they would have been in isolation. Additionally, the induced velocity component becomes negligible compared to the free-stream velocity at high advanced ratios. This determines the indistinguishable difference in propeller performance curves towards the higher end of advance ratios.

As blade spacing reduces, the aerodynamic interference between the blades becomes more significant. The fore (leading) blade imposes an increased downwash on the aft (trailing) blade, while the trailing blade induces an additional upwash on the leading blade. From Figures 13 and 14, it is apparent that the aerodynamic interference effects downstream caused by convected wake vorticity and bound circulation of the leading blade are superior to those upstream caused mainly by the bound vortex of the aft blade. Consequently, the net effect of the reduced blade spacing on the overall induced velocity is increased downwash.

The increase in downwash reduces the effective angle of attack. This ultimately results in a decline in the magnitude of the lift vector and causes the lift vector to tilt forward to remain perpendicular to the local flow, resulting in a decrease in the induced power. This explains the observed behaviour of the performance curves.

An additional set of plots was obtained to show blade spacing effects on the trailing blade aerodynamic performance. Figure 15 illustrates the thrust and power coefficients of the trailing blade, and Figure 16 depicts propulsive efficiency.

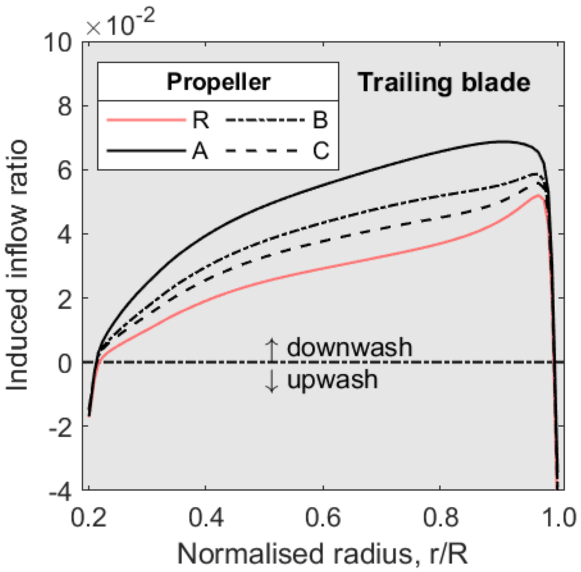

Figure 13 Comparison of the induced inflow ratio acting on the trailing blade between reference propeller "R" and asymmetric propellers "A", "B", and "C" at a collective setting of 20 degrees and an advance ratio of 0.60.

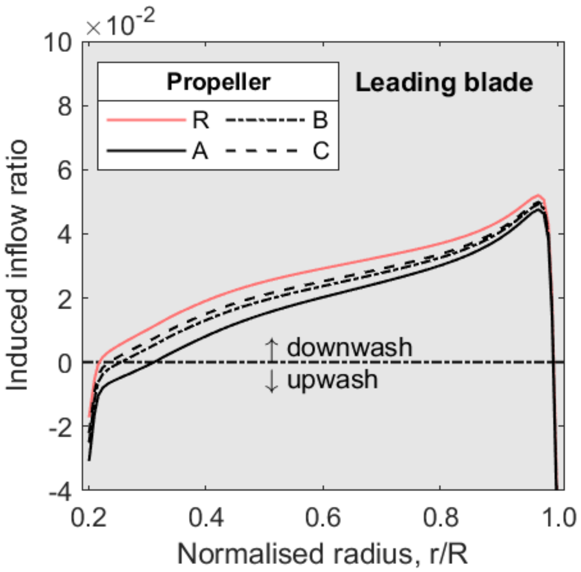

Figure 14 Comparison of the induced inflow ratio acting on the leading blade between reference propeller "R" and asymmetric propellers "A", "B", and "C" at a collective setting of 20 degrees and an advance ratio of 0.60.

The results indicate that the effects of blade spacing on the performance of the trailing blade are comparable to those observed for the overall performance of the propeller. However, as anticipated, the extent of these effects appears to have been amplified.

Overall, the trailing blade is more susceptible to blade spacing. More attention should be given to this aspect if designing an asymmetric propeller.

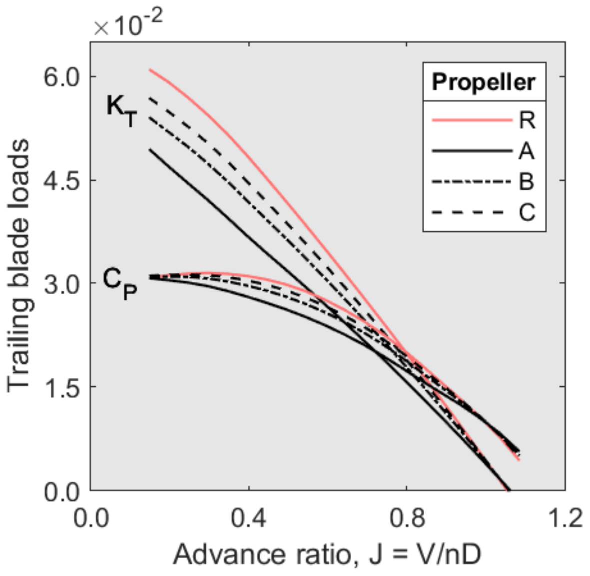

Figure 15 Trailing blade loads comparison between reference "R" and asymmetric "A", "B", and "C" propellers at a collective setting of 20 degrees.

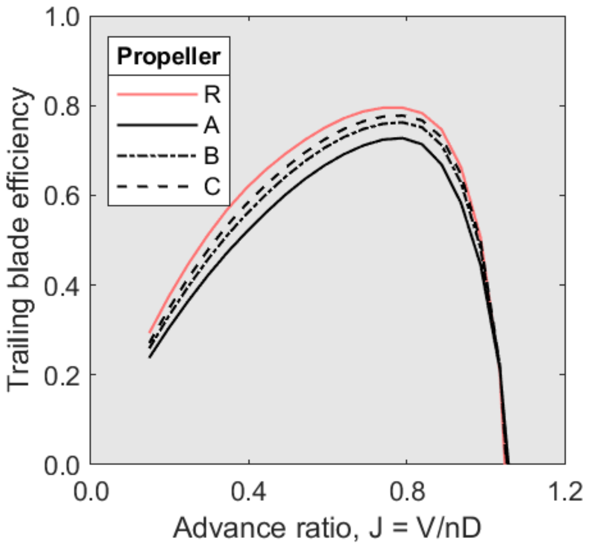

Figure 16 Trailing blade efficiency comparison between reference "R" and asymmetric "A", "B", and "C" propellers at a collective setting of 20 degrees.

5.2. Tip loss and wake geometry

According to classical theory, reducing the normal separation distance between two consecutive vortex sheets should reduce tip loss. Observing whether this postulate applies to the propeller geometries discussed in this study is useful.

Referring to Figure 13, as the blade spacing decreases, the radial distribution of the induced inflow appears to be more uniform. This suggests that tip-loss effects should diminish just as if more blades are added to the propeller.

Figure 17 shows the radial thrust distribution to emphasise the impact of tip-loss effects. The comparative plot indicates that the section thrust declines as the blade spacing decreases, which agrees with the previously described results on induced inflow. However, the magnitude of the thrust alone is not indicative of the tip loss. It can be noticed that the apex of the section thrust coefficient shifts outboard as the blade spacing is reduced. This can be interpreted as an increase in effective blade radius, confirming a tip loss reduction.

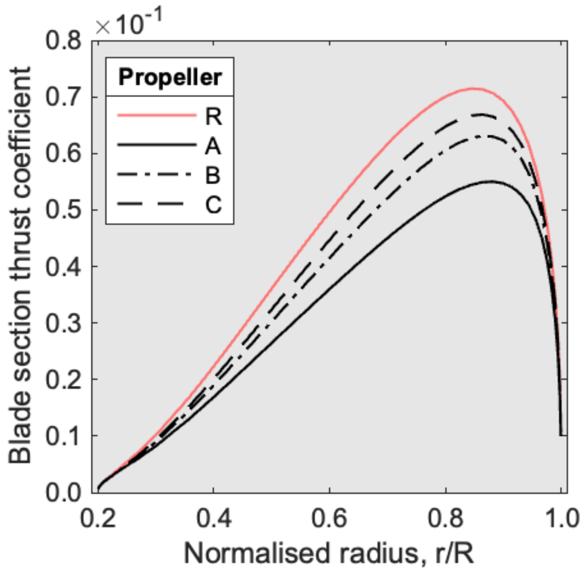

Figure 17 Comparison of the trailing blade's section thrust coefficient between reference propeller "R" and asymmetric propellers "A", "B", and "C" at a collective setting of 20 degrees and an advance ratio of 0.60.

The simulated wake geometries were assessed to understand the underlying reason for this effect better. Figures 18 - 20 show full wake-span geometries of asymmetric propellers truncated at three revolutions. The reference propeller wake geometry is illustrated in Figure 21 for comparison.

When all other parameters are held constant, the distance between two adjacent vortex sheets is determined by the separation of the blades, as anticipated. This provides insights into the origins of the reduced tip loss of the trailing blade. Although not shown here, the leading blade does not experience any change in tip loss due to the blade spacing.

An unexpected result emerges that is worth mentioning: the leading blade vortex sheet rolls inward and eventually encapsulates the vortex sheet released by the trailing blade. The blade spacing angle determines the point where two vortex sheets fully merge to form a unified vortex-sheet structure as if the propeller would only have a single blade. For the asymmetric propeller "A" with the smallest blade spacing, the location at which two vortex sheets become visually indistinguishable lies around half a revolution downstream. As blade spacing increases to 60 and 90 degrees, the point at which wakes merge shifts to ~1.5 and ~2.5 revolutions, respectively.

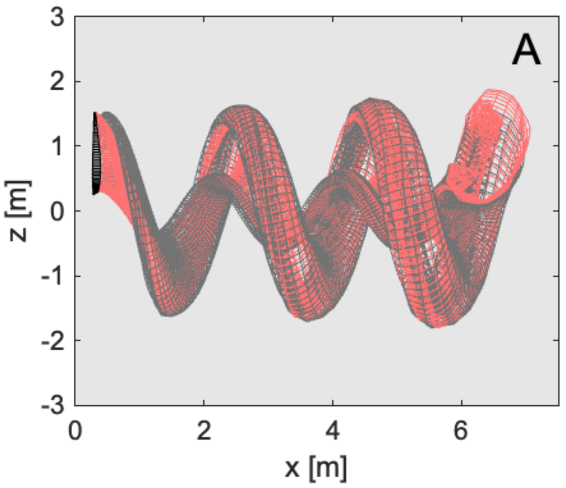

Figure 18 Wake geometry of the asymmetric propeller "A" operating at a collective setting of 20 degrees and an advance ratio of 0.60.

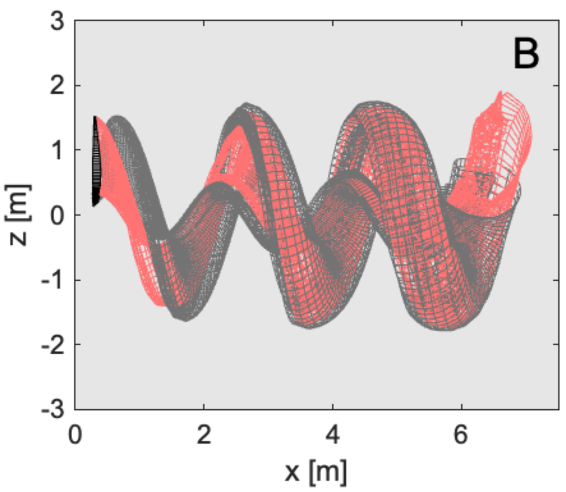

Figure 19 Wake geometry of the asymmetric propeller "B" operating at a collective setting of 20 degrees and an advance ratio of 0.60.

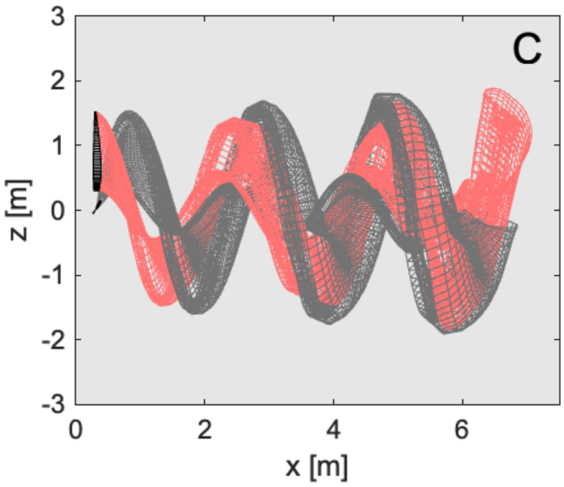

Figure 20 Wake geometry of the asymmetric propeller "C" operating at a collective setting of 20 degrees and an advance ratio of 0.60.

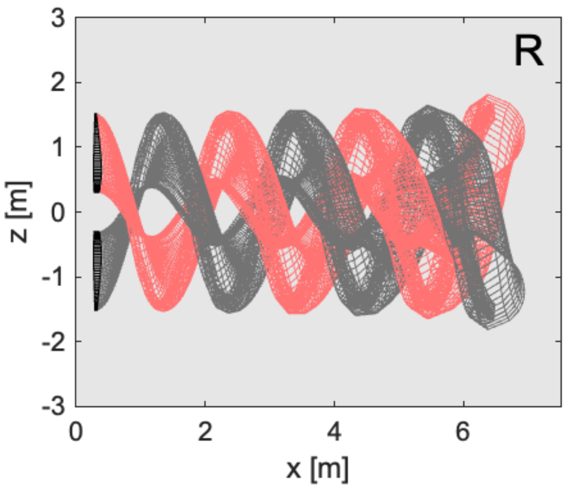

Figure 21 Wake geometry of the reference propeller "R" operating at a collective setting of 20 degrees and an advance ratio of 0.60.

6. CONCLUDING REMARKS

The performance analysis of asymmetric propellers with different blade spacing was presented in this study and compared to a symmetric propeller with evenly spaced blades for reference.

The findings of this work suggest that in asymmetric propellers, the blade spacing affects the performance of individual blades. However, the overall performance of the propeller is marginally affected, especially at higher advance ratios. A reduced blade spacing increases the downwash on the trailing blade, accompanied by a decline in performance. The opposite effect occurs on the leading blade but to a lesser extent. Therefore, the overall propeller performance slightly degrades. Further, results indicate an increase in effective blade radius with a reduction in blade spacing, despite an overall increase in downwash.

To conclude, it is currently unknown to which extent these propellers offer improved acoustic characteristics. However, if this improvement is considerable, it would be sensible to use uneven-asymmetric propellers since their performance is not significantly impacted in comparison to the reference propeller geometry.

The wake geometries indicate that vortex sheets released by the blades merge in an intricate pattern, which could be ground for future work on the aerodynamic interference between multiple asymmetric propellers. The performance of such propeller geometries under edgewise flight operating conditions also holds a prospect for further investigation.

Authors contact:

Dima Usov dmitrij.usov@manchester.ac.uk

7. APPENDIX

Table A1: Summary of percentage errors.

Parameter	K_T	C_P	η
MPE(P,S)	4.85	-1.04	5.46
MAPE(P,S)	4.88	2.88	5.46
MPE(E,P)	-0.01	-0.10	-0.01
MAPE(E,P)	1.12	1.38	0.83

[a] (P,S): fitted polynomial values and simulation results
[b] (E,P): experimental data and fitted polynomial value

8. ACKNOWLEDGEMENTS

This research is funded by the U.K. Engineering and Physical Sciences Research Council (EPSRC) Grant EP/W010119/1 Greener Aviation with Advanced Propulsion Systems (GAAPS).

9. REFERENCES

[1] A. Filippone and G. N. Barakos, “Rotorcraft systems for urban air mobility: A reality check,” *Aeronaut. J.*, vol. 125, no. 1283, pp. 3–21, Jan. 2021, doi: 10.1017/aer.2020.52.

[2] W. Dobrzynski, “Propeller Noise Reduction by Means of Unsymmetrical Blade-spacing,” *J. Sound Vib.*, vol. 163, no. 1, pp. 123–126, May 1993, doi: 10.1006/jsvi.1993.1152.

[3] M. Boltezar, M. Mesaric, and A. Kuhelj, “THE INFLUENCE OF UNEVEN BLADE SPACING ON THE SPL AND NOISE SPECTRA RADIATED FROM RADIAL FANS,” *J. Sound Vib.*, vol. 216, no. 4, pp. 697–711, Oct. 1998, doi: 10.1006/jsvi.1998.1707.

[4] M. Ghoreyshi, P. Aref, C. F. Wisniewski, J. Seidel, and K. W. Van Treuren, “Computational investigation of quiet propeller designs for small unmanned aerial vehicles,” *Aerosp. Sci. Technol.*, vol. 138, p. 108351, Jul. 2023, doi: 10.1016/j.ast.2023.108351.

[5] E. P. Hartman and D. Biermann, “Comparison of Full-Scale Propellers Having R. A. F. 6 And Clark-Y Airfoil Sections,” Langley Field, VA, 1938.

[6] F. Dehaeze and Leonardo Helicopters, “The UK Vertical Lift Network and the MENtOR Project,” 2021.

[7] D. Usov, W. Appleton, A. Filippone, and N. Bojdo, “Low-Order Aerodynamic Model for Interference in Multirotor Systems,” *J. Aircr.*, vol. 59, no. 6, pp. 1450–1462, Nov. 2022, doi: 10.2514/1.C036797.

[8] G. H. Vatistas, V. Kozel, and W. C. Mih, “A simpler model for concentrated vortices,” *Exp. Fluids*, vol. 11, no. 1, pp. 73–76, Apr. 1991, doi: 10.1007/BF00198434.

[9] M. J. Bhagwat and J. G. Leishman, “Correlation of Helicopter Rotor Tip Vortex Measurements,” *AIAA J.*, vol. 38, no. 2, pp. 301–308, Feb. 2000, doi: 10.2514/2.957.

[10] O. Sugar Gabor, “Nonlinear Lifting-Line Model using a Vector Formulation of the Unsteady Kutta-Joukowski Theorem,” *INCAS Bull.*, vol. 11, no. 1, pp. 189–203, Mar. 2019, doi: 10.13111/2066-8201.2019.11.1.15.

[11] J. G. Leishman, *Principles of Helicopter Aerodynamics*, 2nd ed. 2006.

[12] A. I. J. Forrester, A. Sóbester, and A. J. Keane, *Engineering Design via Surrogate Modelling*. Wiley, 2008.

[13] D. Gorissen, I. Couckuyt, E. Laermans, and T. Dhaene, “Multiobjective global surrogate modeling, dealing with the 5-percent problem,” *Eng. Comput.*, vol. 26, no. 1, pp. 81–98, Feb. 2010, doi: 10.1007/s00366-009-0138-1.